ACS APPLIED OPTICAL MATERIALS

pubs.acs.org/acsaom

Article

Wavefront Engineering and Polarization Dynamics in Biological Glass Fibers

Kian M. M. Goeloe,* Igor Zlotnikov, and Lyubov V. Amitonova

Cite This: ACS Appl. Opt. Mater. 2026, 4, 421−428

Read Online

ACCESS | Metrics & More | Article Recommendations

ABSTRACT: Optical fibers are commonly used in different applications, such as data transmission and deep-tissue microscopy. Their small size and flexibility allow access to otherwise hard-to-reach areas. However, the fabrication process of these optical fibers, among other things, requires high temperatures and advanced processing methods, leading to substantial energy costs. A sustainable alternative can be found in nature. Specifically, sponges from the classes *Hexactinellida* and *Demospongiae* form endoskeletal structures comprising individual glass elements called spicules. In many cases, these spicules resemble microscopic fibers. Research has shown that long fiber-like spicules from *Hexactinellid* sponges exhibit a high-refractive-index core, surrounded by a lower refractive index cladding, thus forming an optical waveguide. Here, we demonstrate that sponge spicules from the *Demospongiae* class possess properties that can be utilized in fiber-based applications. In particular, we report the polarization dynamics and spatial wavefront shaping through needle-like spicules from the *Tethya aurantium* sponge. These biologically formed glass elements spark interest because they provide a sustainable and a cost-effective alternative to optical fibers' fabrication.

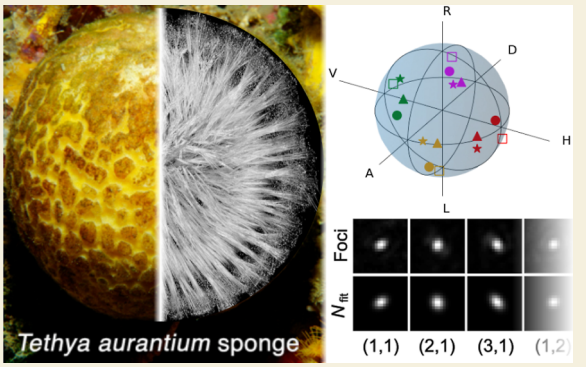

KEYWORDS: *optical fiber, biological glass fiber, sponge, T. aurantium, spicule, polarimetry, wavefront shaping*

INTRODUCTION

Optical waveguides play a central role in modern photonics, enabling precise control and guidance of light for a wide range of applications from data transmission to optical sensing.[1−3] Given the small dimensions at which optical waveguides can be produced, waveguides, and especially optical fibers, are sought-after tools in the field of micro-optics and are commonly applied for in vivo medical procedures such as endomicroscopy. In particular, multimode fibers (MMFs) are well-suited for imaging applications.[4,5] A conventional concept in MMF imaging is based on wavefront shaping, controlling the spatial light field transmitted through complex scattering media.[6] In MMFs, wavefront shaping is achieved by using speckle patterns produced by the simultaneous excitation of several modes in the fiber. Assuming that the MMF can be described as a linear system, any spatial light field can be generated at its output, as has been demonstrated for a variety of solid-core and hollow-core fibers.[7−9] By combining an MMF with wavefront shaping or speckle-based compressive sensing,[10,11] it is possible to create a hair-thin endoscope capable of navigating even the most delicate tissues, such as the brain.[12] This approach enables high-resolution imaging with minimal damage to the surrounding structures.

Nowadays, the majority of optical fibers are silica-based and must be fabricated at high temperatures, which in turn is correlated with high energy costs.[13,14] Sustainable alternatives to conventional fabrication methods can be found in the form of spider silk,[15] silkworm silk,[15,16] biopolymers,[17,18] and sponges where the organisms form species-specific 3D macroscopic glass assemblies in vivo under ambient physiological conditions through a bottom-up approach:[19] without high temperatures, toxic chemicals, or significant energy input. The biologically grown structures of the latter not only offer a sustainable alternative to optical fiber fabrication but may also provide improved compatibility with bioimaging applications and will be the main focus of this work.

Hexactinellida and *Demospongiae* are two sponge classes from the phylum *Porifera* that form their skeletons from individual microscopic glass (amorphous silica) elements—the spicules. The morphology of the sponges and the spicules varies, serving a wide range of functions, such as structural rigidity, anchoring to substrates, and even waveguide properties. Nevertheless, regardless of their overall shape, the spicules in both classes

Received: November 17, 2025
Revised: February 9, 2026
Accepted: February 10, 2026
Published: February 18, 2026

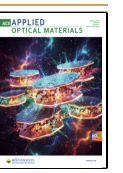

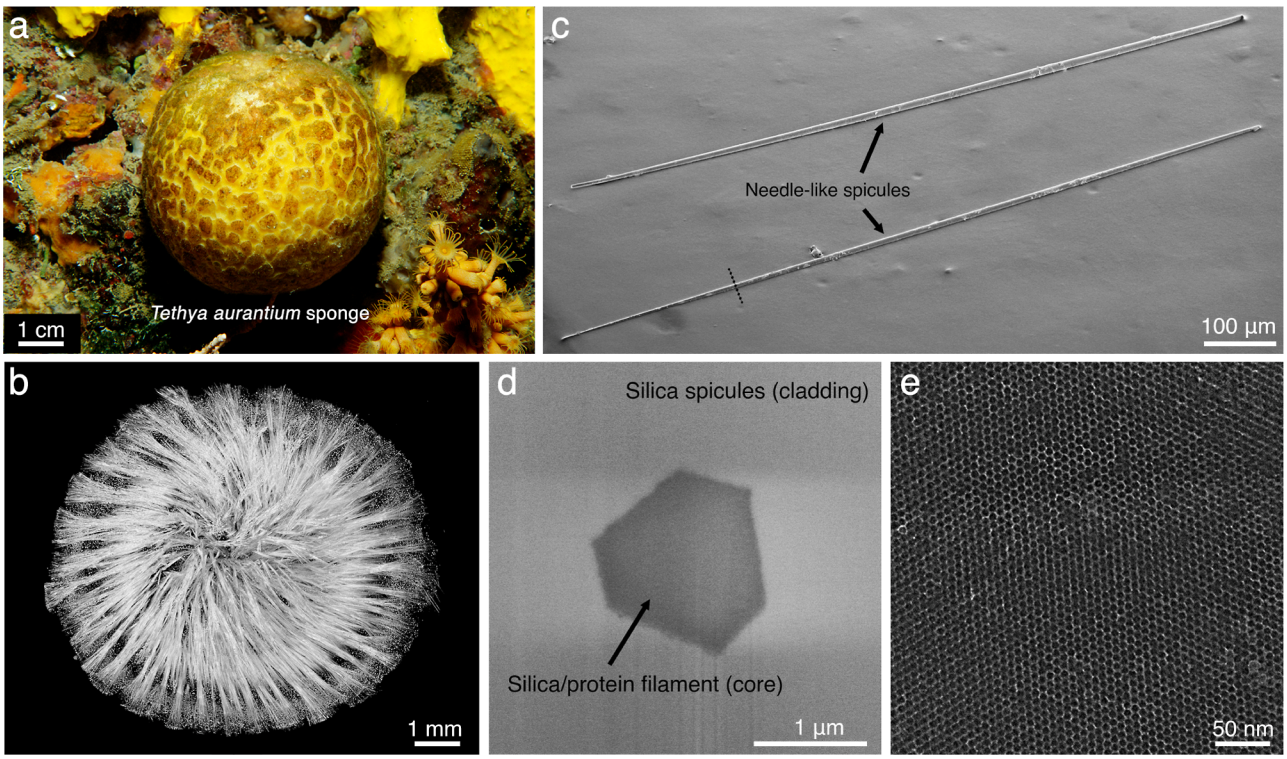

Figure 1. Glass skeleton of the sponge *Tethya aurantium*. (a) The *demosponge T. aurantium*. (b) 3D structure of the mineralized silica skeleton in *T. aurantium* obtained using X-ray microtomography. (c) Needle-like spicules extracted from the sponge *T. aurantium* used in this study. (d) A section through a needle-like spicule obtained using a Focused Ion Beam (FIB) milling method (marked by a dashed line in (c)) depicting the presence of a highly ordered silica/protein filament passing through the center of the spicule. (e) Transmission Electron Microscopy (TEM) image of the filament underlying the crystalline nature of the axial filament. The hybrid silica/protein crystal has a hexagonal unit cell belonging to the symmetry group $P3_121$ with a = 5.96 nm and c = 11.63 nm as portrayed by the hexagonal habit of the filament in (d). The c-axis of the hybrid is parallel to the long axis of the spicules. The image was obtained on a sample lifted out from the spicules using FIB. The imaging direction is parallel to the long axis of the needle.[19]

harbor an axial filament passing through the center of the spicules.[19−24] The filament, having a diameter of up to 2 μm, is a hybrid protein/mineral composite made of proteins and silica assembled into highly periodic crystal-like superstructure.[19,25] However, while the material surrounding the filament in *Demosponges* is a bulk biogenic glass,[19] in *Hexactinellids*, the spicules first comprise a relatively thick glass tube and then concentric glass cylinders, enveloping the axial filament.[20] Interestingly, fiber-like spicules from the latter were already demonstrated to guide light, functioning as natural optical waveguides that support both single-mode and multimode transmission. For example, Aizenberg et al. have demonstrated that spicules originating from the *Hexactinellid Euplectella aspergillum* and used to anchor the sponge to soft sediment[26] are capable of guiding light through its core and cladding.[20] More recent work has shown that it is possible to efficiently couple laser light into spicules extracted from another *Hexactinellid*, the *Sericolophus hawaiicus* glass sponge. Furthermore, it has been depicted that these spicules are capable of supercontinuum generation due to their internal structure having similarities to artificially made fibers used specifically for this purpose.[21] All previous examples have demonstrated light propagation through spicules from *Hexactinellid* sponges. In this work, we demonstrate that spicules of the *Demosponges* class have similar characteristics and can be used for fiber-based applications.

Demosponges live in most aquatic habitats and are the most diverse *Porifera* class, comprising about 85% of all existing sponge species.[27] In particular, we study the light-guiding properties, birefringence, and wavefront shaping in needle-like spicules from the sponge *Tethya aurantium*, also known as the orange puffball sponge (Figure 1a). These spicules form the organism's supportive skeleton, radiating isotropically from the sponge center (Figure 1b). An individual spicule can reach ≈2 mm in length and >30 μm in diameter (Figure 1c).[19,28] Every spicule contains the afforded micrometer-sized faceted axial filament (the core, Figure 1d), reflecting its crystalline ultrastructure (Figure 1e), surrounded by bulk amorphous biosilica (the cladding, Figure 1d). Waveguide potential of the spicules has been observed by Brummer et al.,[29] using photosensitive paper material inserted into living *T. aurantium* sponges. Furthermore, earlier research suggested that light conduction through needle-like spicule bundles facilitates an unusual association of *Cyanobacteria* with the sponge endosome.[30]

The structure of this paper is as follows: first, the preparation of the spicule sample and the key factors that need to be taken into account for coupling monochromatic light into the spicule are discussed. This is followed by a description of the experimental setup and configuration to explore the optical properties of the *T. aurantium* spicule. Next, the results of the polarimetry and wavefront shaping on the spicule are presented and discussed in relation to the material properties. Finally, the results are summarized, and a possible outlook of this research is discussed.

https://doi.org/10.1021/acsaom.5c00572
ACS Appl. Opt. Mater. 2026, 4, 421−428

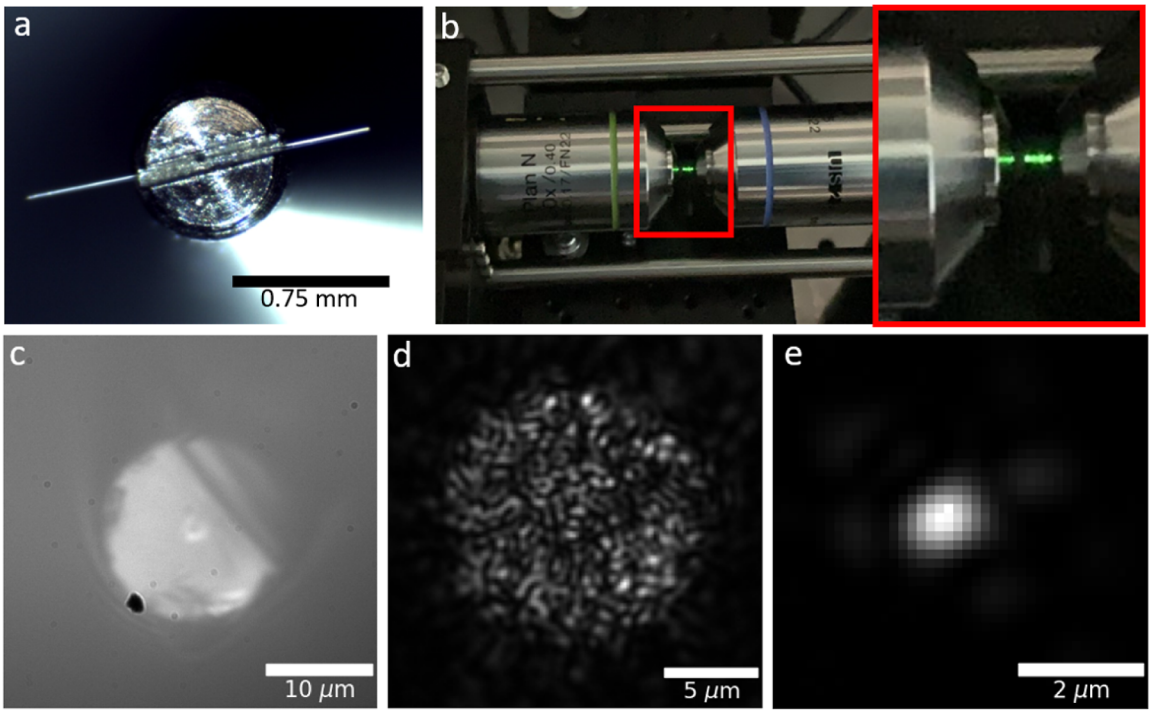

Figure 2. Light coupling into the *T. aurantium* spicule. (a) Single spicule extracted from the *T. aurantium* sponge resting on a custom-made sample holder. (b) Monochromatic light at $\lambda = 532$ *nm* coupling into the spicule. Inset shows an additional reflection of the spicule on the left objective. (c) Microscopic image of the input facet of the spicule using an incoherent light source. (d) Image of the speckle pattern at the output facet of the spicule when resting in free space. (e) Image of the fiber core profile at the output facet of the spicule embedded in a high-refractive-index medium.

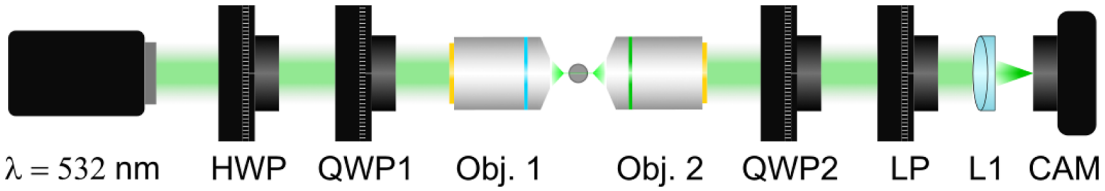

Figure 3. Schematic view of the polarimetry experimental setup. Monochromatic light ($\lambda = 532$ *nm*) passes through the half-waveplate (*HWP*) and the quarter-waveplate (*QWP*) to control the input polarization. Subsequently, the light is coupled into the spicule and collected from the spicule with two objectives (see Figure 2c,e). Thereafter, the evolved polarization state is extracted by means of the QWP and the linear polarizer (*LP*).

METHODS

Spicule

A segment from a *T. aurantium* sponge is treated with 5% (v/v) sodium hypochlorite solution until all of the organic material surrounding the spicules is removed. The residual mass containing the spicules is rinsed five times with Milli-Q water and two times with 95% ethanol and finally air-dried.[23] A single spicule is extracted under a stereo microscope and placed on the sample holder with both ends protruding (Figure 2a). Due to the micrometer dimensions of a single spicule, a custom-designed tip sample holder with a narrow slit on top is fabricated, compatible for coupling light into the spicule core without impeding the acceptance cone (Figure 2b). The spicules are as is without polishing or any other mechanical modifications.

Light Coupling

Coupling light into the spicule is accomplished by having the input facet of the spicule in the image plane of objective 1 (Olympus Plan N, 40×, NA = 0.65). The output facet of the spicule is placed in the image plane of objective 2 (Olympus Plan N, 20×, NA = 0.4) to collect the exiting light. The described coupling and collection objectives are denoted as Obj.1 and Obj.2 as shown in Figure 3, respectively. The spicule in combination with a monochromatic light source (Cobolt Samba Nd:YAG) at wavelength $\lambda = 532$ nm allows for a large number of modes to be propagated, which is additionally attributable to the refractive index contrast between the cladding of the spicule and the surrounding air, allowing cladding modes to exist (Figure 2d). This behavior corresponds to a biological MMF, now acting as a random scattering medium. The cladding modes can be suppressed by embedding the spicule in a medium with a high refractive index ($n_{clad} < n_{med}$), effectively transmitting any light propagating through the cladding into the surrounding medium or coupled into the spicule core.[20] As a high-refractive-index media, we use the Norland Optical Adhesive NOA 61 ($n = 1.56$). The resulting single-/few-mode profiles originating solely from the core are shown in Figure 2e. The optical transmission of the spicule waveguide was characterized by measuring the input and output optical power using a Thorlabs S121C Photodiode power sensor combined with Thorlabs PM100D power meter. After calibrating the transmission of the coupling and collection optics and the combined setup efficiency including NA mismatch ($\rho_{setup} = 0.4$), the intrinsic transmission of the spicule was determined to be $\rho = 0.23$ in free space and $\rho = 0.2$ when embedded in a high-refractive-index adhesive.

Polarimetry Setup

The setup given in Figure 3 is designed to obtain polarization information using Stokes polarimetry by means of a combination of waveplates and a polarizer. The half-waveplate (Thorlabs AHWP10M-600) and the quarter-waveplate (Thorlabs AQWP10M-580) prior to the spicule allow for controlling the incident polarization

https://doi.org/10.1021/acsaom.5c00572
ACS Appl. Opt. Mater. 2026, 4, 421−428

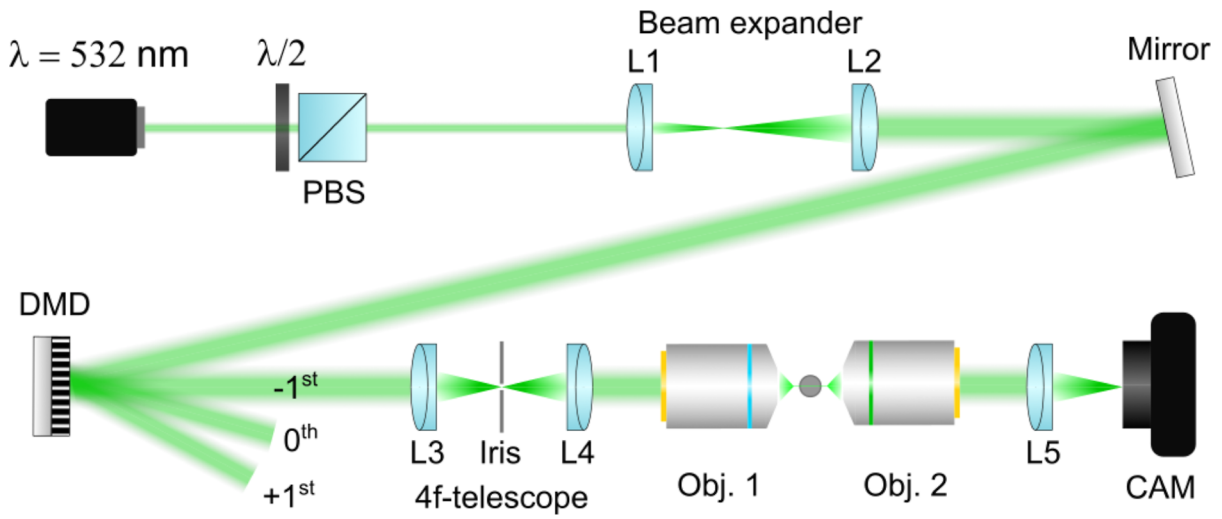

Figure 4. Schematic view of the wavefront shaping experimental setup. Monochromatic light (λ = 532 *nm*) passes through the half-waveplate (*HWP*) and polarizing beam splitter (PBS) to control the laser power. The beam spot size is expanded by a combination of two lenses (*L*1 and *L*2) for optimal coverage on the digital micromirror device (DMD). The −1st diffraction order is isolated by means of a pinhole resting within the 4f-system consisting of lenses *L*3 and *L*4. Subsequently the light is coupled into the spicule and collected from the spicule by two objectives. The light collected from the spicule is imaged on the camera (see Figure 2c,d).

and are denoted by *HWP* and QWP1, respectively. The quarter waveplate (Thorlabs AQWP10M-580) and linear polarizer (Thorlabs LPVISE100-A) subsequent to the spicule allow resolving of the evolved polarization state and are denoted by QWP2 and *LP*, respectively. The Stokes parameters S_0, S_1, S_2, and S_3 are extracted by taking 6 intensity images with the waveplates and polarizer at different rotational configurations, following the convention outlined in ref 31. The S_0 parameter denotes the total intensity, and S_1, S_2, and S_3 quantify the balance between orthogonal states: horizontal ($|H\rangle$) and vertical ($|V\rangle$) polarization, diagonal ($|D\rangle$) and antidiagonal ($|A\rangle$) polarization, and right-handed ($|R\rangle$ and left-handed ($|L\rangle$) circular polarization, respectively. To extract any information regarding the birefringence of the spicule core, the spicule is embedded in a high-index medium (Norland Optical Adhesive NOA 61, n = 1.56) to avoid polarization scrambling between the core and cladding modes. The output facet is imaged on the camera (Basler acA3088 − 57 μm) with a tube lens (Thorlabs AC254-200-A-ML), denoted by L1 in Figure 3. For calculating the Stokes parameters in postprocessing, each image corresponding to a particular configuration of QWP2 and *LP* is integrated to one single intensity value.

Wavefront Shaping Setup

The setup for wavefront shaping experiments is given in Figure 4 and equipped with a 1920 × 1200 Digital Micromirror Device (Texas Instruments) and driven by the DLP V-9500 VIS module (ViALUX), which allows for wavefront shaping using speckle patterns by means of phase control, following the convention described in ref 32. The spicule rests on the sample holder in free space, allowing for core and cladding modes to propagate, which give rise to speckle patterns. The laser is incident on the DMD in such a way that the -1^{st} diffraction order, which contains the phase pattern information, can be isolated using a pinhole resting within a 4f-system consisting of L3 (Thorlabs AC508-150-A-ML) and L4 (Thorlabs AC254-100-A-ML). Thereafter, the modulated light is coupled into the spicule with objective 1 (Olympus Plan N, 20×, NA = 0.4), and the light exiting the spicule is collected by objective 2 (Leica HCX PL Fluotar, 40×, NA = 0.60), denoted by Obj. 1 and Obj. 2 in Figure 4, respectively. Finally, the image of the spicule output facet is projected onto the camera (Basler acA640-750 μm) with tube lens L5 (Thorlabs AC254-050-A-ML). A beam expanding telescope system consisting of L1 (Thorlabs AC254-50-A-ML) and L2 (Thorlabs AC254-150-A-ML) is used prior to the DMD to expand the modulation area, and the laser power is regulated by using a combination of a half-waveplate and a polarizing beamsplitter (Thorlabs VA5-532/M).

RESULTS AND DISCUSSION

Polarization Evolution in the Core

In the first set of experiments, we investigate polarization evolution in the *T. aurantium* sponge spicule core (the filament). Several polarimetry measurements on different spicules are performed to inquire into the polarization evolution of monochromatic light through the spicule core as a function of the propagation distance. The spicules with lengths of 0.8 mm, 1.64 mm, and 1.75 mm have been investigated. For each sample, 4 different input polarizations ($|H\rangle$, $|V\rangle$, $|R\rangle$, and $|L\rangle$) are configured. Additionally, a measurement without a spicule sample is performed as a reference to validate the polarimetry setup and identify potential offsets within the system. The results are graphically shown in a Poincaré sphere, where the color denotes the configured input polarization, and the symbols indicate the spicule sample length (L) (Figure 5).

Assuming that any form of birefringence is present in the spicule due to either the spicule core material or the structure, the output polarization should change with respect to the input polarization according to the spatial direction of the birefringence. The evolved polarization state in the (S_1, S_3) plane undergoes a systematic clockwise-rotation when comparing the longest spicule to the shortest. However, the measured output polarization states for different species show no clear significant variation. As shown in Figure 5, the corresponding points on the Poincaré sphere cluster closely together, indicating that any polarization evolution during propagation is either weak or below the detection sensitivity of our setup. While the presence of a spicule alters the polarization ellipticity and purity compared to the reference measurement without a sample, the cumulative effect remains minimal across the range of spicule lengths studied. This suggests that the intrinsic birefringence of the spicule is low.

Wavefront Shaping

In the final set of experiments, we performed wavefront shaping through the core and cladding of the *T. aurantium* sponge spicule using the setup given in Figure 4 with the

https://doi.org/10.1021/acsaom.5c00572
ACS Appl. Opt. Mater. 2026, 4, 421−428

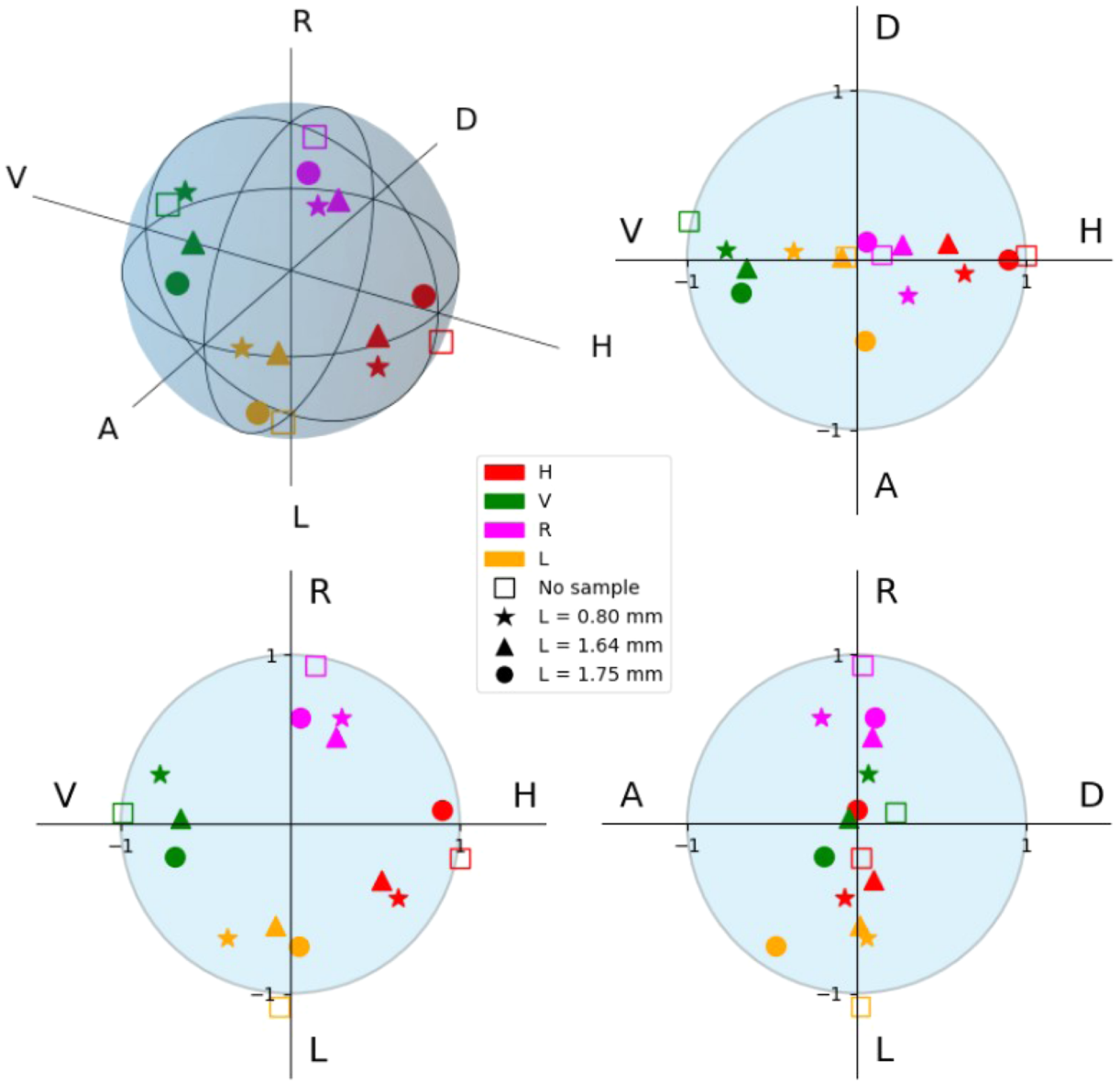

Figure 5. Poincaré spheres showing the polarimetry measurement results on the spicule core. Upper-left: 3D representation of the polarimetry results. Upper-right: 2D projection of the polarimetry results in the (S_1, S_2) plane. Lower-left: 2D projection of the polarimetry results in the (S_1, S_3) plane. Lower-right: 2D projection of the polarimetry results in the (S_2, S_3) plane. The colors denote the configured input polarization, and symbols correspond to different spicule samples with different lengths.

spicule positioned in free space on the sample holder and not embedded in high-refractive-index glue. In this configuration, the spicule exhibits multimodal behavior in the core and cladding, resulting in the formation of speckle patterns. Using Lee holography, the DMD is configured to generate 12 distinct foci on the output facet of the spicule (Figure 6a). The active modulation area is set to 500 × 500 mirrors, subdivided into 30 × 30 segments. To measure the spicule's transmission matrix, each segment on the DMD is sequentially modulated with three different but equidistant phases (0π, $2/3\pi$, $4/3\pi$), leaving the remaining segments acting as the reference phase (Figure 6b). This procedure results in a set of speckle patterns that are used to calibrate the modulation phases for each segment to maximize the intensity at the desired focal spot positions. Ultimately, a focal spot on the output facet of the spicule is generated when all precalibrated segments on the DMD are active. The results of the 12 foci on the output facet of the spicule are summarized in Figure 6c, by extracting the maximum intensity of each pixel from all images of the foci. The lower-left focal spot is labeled (1,1) and the upper-right focal spot is denoted as (3,4), with the remaining foci indexed accordingly, following this coordinate system. In Figure 6d, the individual foci are shown, each cropped to a 40 × 40 pixel region centered on the focus and normalized to its local maximum intensity to present the shape and structure of each optimized focus. To evaluate the quality of wavefront shaping, the power ratio for each of the foci is used as a figure of merit and is calculated by fitting each focal spot with a 2D Gaussian profile (N_{fit}), and applying eq 1:

$$\eta \equiv \frac{I_{\text{FWHM}}}{I_{\text{tot}}} \cdot 100\% \tag{1}$$

where η denotes the power ratio of the focal spot, I_{FWHM} indicates the intensity measured at twice the full width half-

https://doi.org/10.1021/acsaom.5c00572
ACS Appl. Opt. Mater. 2026, 4, 421−428

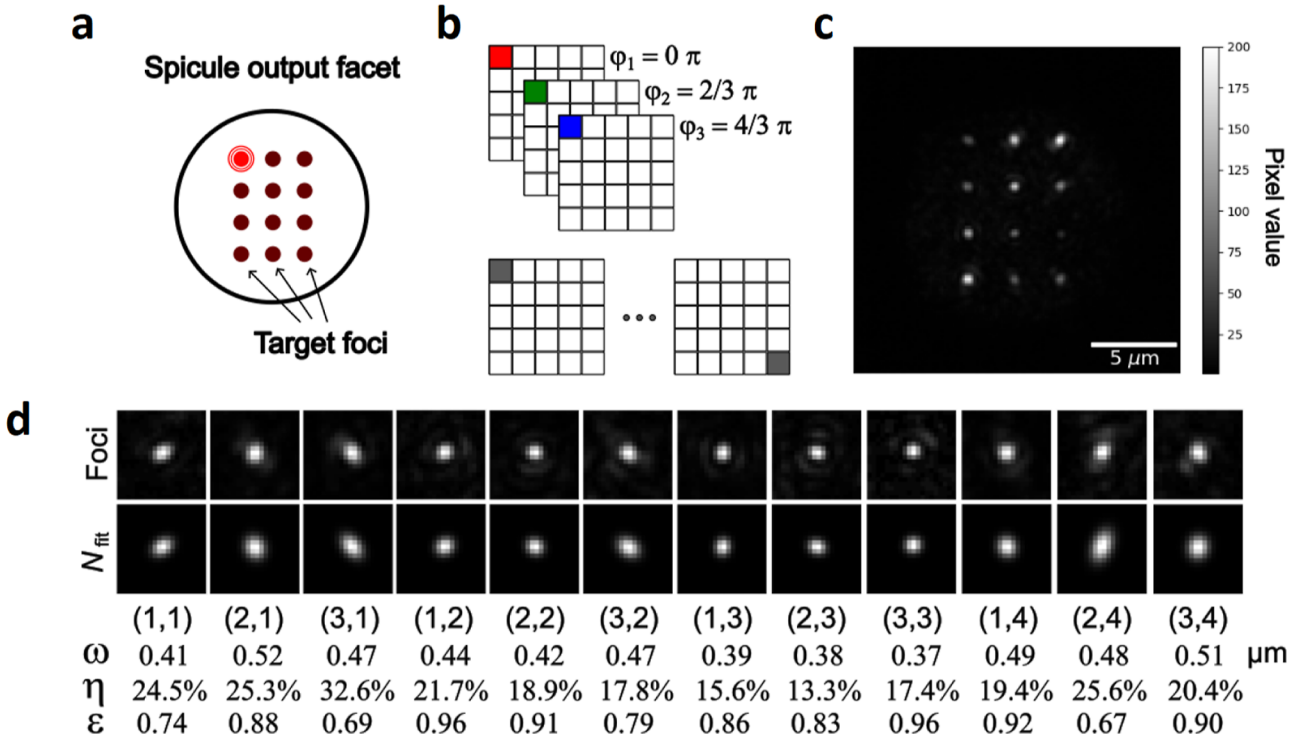

Figure 6. Results of wavefront shaping through the spicule core and cladding. (a) Schematic drawing of the target positions of the 12 optimized foci on the output facet of the spicule. (b) Illustrative representation of the phase modulation of each segment on the DMD during the wavefront shaping procedure for the highlighted target position in Figure 6a. (c) Maximum intensity projection of 12 optimized foci on the output facet of the spicule. (d) Individual focal spots, optimized on the output facet of the spicule, each normalized, cropped, and centered on the focus for individual quality analysis. ω, η, and ϵ denote the minimum width of N_{fit} at FWHM, the power ratio of the foci, and the roundness of N_{fit}, respectively.

maximum (FWHM) of the focal spot, and I_{tot} denotes the total intensity of the full image. It is important to note that the use of phase-only modulation combined with single polarization modulation limits the maximum achievable power ratio to approximately 40%. The resulting power ratio of each foci is shown in Figure 6d. The average power ratio of all foci is determined to be 21.0 ± 5.0%, where the uncertainty represents one standard deviation, 1σ. We note that under the present conditions the PR is primarily determined by the experimental implementation rather than the intrinsic limitations of the spicule. Under the same experimental settings, power ratios of up to approximately 30% have been shown for a conventional MMF.[33] The results indicate that the spicule performance in wavefront shaping is similar to that of man-made optical fibers. With the full experimental control, which includes both polarization states and simultaneous phase and amplitude modulation, focusing efficiencies approaching 100% have been demonstrated in a conventional MMF.[34]

In addition to calculating the power ratio, the minimum width of N_{fit} at FWHM (ω) is given and the roundness (ε) of N_{fit} is calculated by ω/ω_{max}, with ω_{max} the maximum width of N_{fit}, measured at FWHM. The numerical aperture (NA) plays a central role in determining the resolution of diffraction-limited imaging systems. The results presented in Figure 6 originate from a system in which the resolution ultimately depends on the numerical aperture of the spicule glass cladding. The numerical aperture can be estimated following the expression $NA = \lambda/2\langle w\rangle$, resulting in NA = 0.60 ± 0.07. We note that this value should be interpreted as an effective, lower-bound estimate of the true NA, as incomplete control of the highest-order guided modes may lead to a slight broadening of the focal spot. Given that the refractive index contrast between the cladding and air is larger than the contrast between the core and cladding, it is expected that the numerical aperture of the cladding modes will be significantly larger. However, impurities and inhomogeneities associated with the biogenic origin of spicules[19,25] make the calculation of an accurate theoretical numerical aperture challenging. Despite the complexity of accurately modeling due to biological heterogeneity, the estimated NA is remarkably high and the ellipticity of the foci is well preserved. In summary, we show the feasibility of the spicule to act as a random scattering medium suitable for wavefront shaping methods to control light. This capability introduces a pathway for biological glass fibers to act as sustainable solutions for fiber-based applications.

CONCLUSION

This work establishes a foundational understanding of biological glass fibers as waveguides by investigating their birefringent properties and exploring their applications in wavefront shaping. The glass spicules of *Demosponge T. aurantium* are experimentally studied to assess their potential as optical fibers and to explore the feasibility of biological fibers to act as a sustainable and cost-effective alternative to conventional man-made silica fibers. Our results demonstrate successful and controlled light coupling in the *T. aurantium* spicule core and/or cladding and show its wavefront shaping capability, revealing a remarkably high numerical aperture of 0.60 ± 0.07 and well-preserved ellipticity. In addition, the average power ratio of the foci is determined to be 21.0 ± 5.0%, which is similar to the power ratios measured with man-

https://doi.org/10.1021/acsaom.5c00572
ACS Appl. Opt. Mater. 2026, 4, 421−428

made MMFs in the case of phase-only single polarization wavefront shaping. Although the intrinsic birefringence of the spicule, due to either the material or its structure, can be considered low, these findings highlight biological glass fibers as promising candidates for conventional fiber applications, especially where compactness and advanced light control are desired. However, further research is necessary to fully characterize their optical properties and understand the biological processes that enable glass sponges to precisely control their morphology and waveguiding capabilities. Although the current length of the spicules limits many practical applications, they can already be useful as biocompatible, millimeter-scale implants for minimally invasive in vivo neuroimaging.[35] Moreover, this work provides results on their optical properties, which are relevant for biomimetic approaches and for the fabrication of analogous structures under controlled laboratory conditions. Hence, continued exploration of these natural photonic structures could open new avenues for sustainable, bioinspired fiber technologies.

AUTHOR INFORMATION

Corresponding Author

Kian M. M. Goeloe − *Advanced Research Center for Nanolithography (ARCNL), Amsterdam 1098 XG, The Netherlands; Department of Physics and Astronomy, Vrije Universiteit Amsterdam, Amsterdam 1081 HV, The Netherlands;* orcid.org/0009-0004-5931-380X; Email: k.goeloe@arcnl.nl

Authors

Igor Zlotnikov − *B CUBE - Center for Molecular Bioengineering, Technische Universität Dresden, Dresden 01309, Germany*

Lyubov V. Amitonova − *Advanced Research Center for Nanolithography (ARCNL), Amsterdam 1098 XG, The Netherlands; Department of Physics and Astronomy, Vrije Universiteit Amsterdam, Amsterdam 1081 HV, The Netherlands*

Complete contact information is available at: https://pubs.acs.org/10.1021/acsaom.5c00572

Notes

The authors declare no competing financial interest.

ACKNOWLEDGMENTS

This work was partially conducted at the Advanced Research Center for Nanolithography, a public-private partnership between the University of Amsterdam, Vrije Universiteit Amsterdam, University of Groningen, The Netherlands Organization for Scientific Research (NWO), and the semiconductor equipment manufacturer ASML and was (partly) financed by "Toeslag voor Topconsortia voor Kennis en Innovatie (TKI)" from the Dutch Ministry of Economic Affairs. This work is also supported by the NWO-TTW Perspectief program P21-20 "Optical coherence; optimal delivery and positioning" (OPTIC) in collaboration with TUE, TUD, and UT and with industrial partners Anteryon, ASML, Demcon, JMO, Signify, and TNO. We thank Wessel Zwart for manufacturing the customized tip sample holder.

REFERENCES

(1) Tafur Monroy, I.; Vd Boom, H.; Koonen, A.; Khoe, G.; Watanabe, Y.; Koike, Y.; Ishigure, T. Data transmission over polymer optical fibers. *Optical Fiber Technology* **2003**, *9*, 159−171.

(2) Pendão, C.; Silva, I. Optical Fiber Sensors and Sensing Networks: Overview of the Main Principles and Applications. *Sensors* **2022**, *22*, 7554.

(3) Abrashitova, K.; Amitonova, L. V. Multimode fiber ruler for detecting nanometric displacements. *APL Photonics* **2022**, *7*, 086103.

(4) Cao, H.; Čižmár, T.; Turtaev, S.; Tyc, T.; Rotter, S. Controlling light propagation in multimode fibers for imaging, spectroscopy, and beyond. *Adv. Opt. Photonics* **2023**, *15*, 524.

(5) Amitonova, L. V. Multimode fiber endoscopes for computational brain imaging. *Neurophotonics* **2024**, *11*..

(6) Vellekoop, I. M.; Mosk, A. P. Focusing coherent light through opaque strongly scattering media. *Opt. Lett.* **2007**, *32*, 2309.

(7) Čižmár, T.; Dholakia, K. Shaping the light transmission through a multimode optical fibre: complex transformation analysis and applications in biophotonics. *Opt. Express* **2011**, *19*, 18871.

(8) Lyu, Z.; Amitonova, L. V. Wavefront shaping and imaging through a multimode hollow-core fiber. *Opt. Express* **2024**, *32*, 37098.

(9) Amitonova, L. V.; Descloux, A.; Petschulat, J.; Frosz, M. H.; Ahmed, G.; Babic, F.; Jiang, X.; Mosk, A. P.; Russell, P. S.; Pinkse, P. W. H. High-resolution wavefront shaping with a photonic crystal fiber for multimode fiber imaging. *Opt. Lett.* **2016**, *41*, 497.

(10) Amitonova, L. V.; De Boer, J. F. Endo-microscopy beyond the Abbe and Nyquist limits. *Light:Sci. Appl.* **2020**, *9*, 81.

(11) Amitonova, L. V.; de Boer, J. F. Compressive imaging through a multimode fiber. *Opt. Lett.* **2018**, *43*, 5427−5430.

(12) Stibůrek, M.; Ondráčková, P.; Tučková, T.; Turtaev, S.; Šiler, M.; Pikálek, T.; Jákl, P.; Gomes, A.; Krejčí, J.; Kolbábková, P.; Uhlířová, H.; Čižmár, T. 110 μ m thin endo-microscope for deep-brain in vivo observations of neuronal connectivity, activity and blood flow dynamics. *Nat. Commun.* **2023**, *14*, 1897.

(13) Acquah, C.; Datskov, I.; Mawardi, A.; Zhang, F.; Achenie, L. E. K.; Pitchumani, R.; Santos, E. Optimization of an Optical Fiber Drawing Process under Uncertainty. *Ind. Eng. Chem. Res.* **2006**, *45*, 8475−8483.

(14) Cheng, X.; Jaluria, Y. Optimization of a thermal manufacturing process: Drawing of optical fibers. *Int. J. Heat Mass Transfer* **2005**, *48*, 3560−3573.

(15) Qiao, X.; Qian, Z.; Li, J.; Sun, H.; Han, Y.; Xia, X.; Zhou, J.; Wang, C.; Wang, Y.; Wang, C. Synthetic Engineering of Spider Silk Fiber as Implantable Optical Waveguides for Low-Loss Light Guiding. *ACS Appl. Mater. Interfaces* **2017**, *9*, 14665−14676.

(16) Zhang, Y.; Lu, H.; Zhang, M.; Hou, Z.; Li, S.; Wang, H.; Wu, X.-E.; Zhang, Y. In Situ Mineralizing Spinning of Strong and Tough Silk Fibers for Optical Waveguides. *ACS Nano* **2023**, *17*, 5905−5912.

(17) Patrakka, J.; Hynninen, V.; Huttunen, P.; Nonappa. Nonappa Biopolymer Optical Fibers for High-Sensitivity Quantitative Humidity Monitoring. *ACS Appl. Mater. Interfaces* **2025**, *17*, 49816−49828.

(18) Reimer, M.; Van Opdenbosch, D.; Zollfrank, C. Fabrication of Cellulose-Based Biopolymer Optical Fibers and Their Theoretical Attenuation Limit. *Biomacromolecules* **2021**, *22*, 3297−3312.

(19) Görlich, S.; Samuel, A. J.; Best, R. J.; Seidel, R.; Vacelet, J.; Leonarski, F. K.; Tomizaki, T.; Rellinghaus, B.; Pohl, D.; Zlotnikov, I. Natural hybrid silica/protein superstructure at atomic resolution. *Proc. Natl. Acad. Sci. U. S. A.* **2020**, *117*, 31088−31093.

(20) Aizenberg, J.; Sundar, V. C.; Yablon, A. D.; Weaver, J. C.; Chen, G. Biological glass fibers: Correlation between optical and structural properties. *Proc. Natl. Acad. Sci. U. S. A.* **2004**, *101*, 3358−3363.

(21) Ehrlich, H.; et al. Supercontinuum Generation in Naturally Occurring Glass Sponges Spicules. *Adv. Opt. Mater.* **2016**, *4*, 1608−1613.

(22) Reiswig, H. M.; Mackie, G. O. Studies on hexactinellid sponges. III. The taxonomic status of hexactinellida within the porifera. *Philos. Trans. R. Soc. Lond. B Biol. Sci.* **1983**, *301*, 419−428.

(23) Schoeppler, V.; Reich, E.; Vacelet, J.; Rosenthal, M.; Pacureanu, A.; Rack, A.; Zaslansky, P.; Zolotoyabko, E.; Zlotnikov, I. Shaping

highly regular glass architectures: A lesson from nature. *Sci. Adv.* **2017**, *3*, No. eaao2047.
(24) Kulchin, Y. N.; Bukin, O. A.; Voznesenskii, S. S.; Galkina, A. N.; Gnedenkov, S. V.; Drozdov, A. L.; Kuryavyi, V. G.; Mal'tseva, T. L.; Nagornyi, I. G.; Sinebryukhov, S. L.; Cherednichenko, A. I. Optical fibres based on natural biological minerals — sea sponge spicules. *Quantum Electron.* **2008**, *38*, 51−55.
(25) Schoeppler, V.; Stier, D.; Best, R. J.; Song, C.; Turner, J.; Savitzky, B. H.; Ophus, C.; Marcus, M. A.; Zhao, S.; Bustillo, K.; Zlotnikov, I. Crystallization by Amorphous Particle Attachment: On the Evolution of Texture. *Adv. Mater.* **2021**, *33*, 2101358.
(26) Levi, C.; Barton, J. L.; Guillemet, C.; Le Bras, E.; Lehuede, P. A remarkably strong natural glassy rod: the anchoring spicule of theMonorhaphis sponge. *J. Mater. Sci. Lett.* **1989**, *8*, 337−339.
(27) Wörheide, G.; Dohrmann, M.; Erpenbeck, D.; Larroux, C.; Maldonado, M.; Voigt, O.; Borchiellini, C.; Lavrov, D. *Advances in Marine Biology*; Elsevier, 2012; Vol. *61*, pp 1−78.
(28) Shimizu, K.; Cha, J.; Stucky, G. D.; Morse, D. E. Silicatein α: Cathepsin L-like protein in sponge biosilica. *Proc. Natl. Acad. Sci. U. S. A.* **1998**, *95*, 6234−6238.
(29) Brümmer, F.; Pfannkuchen, M.; Baltz, A.; Hauser, T.; Thiel, V. Light inside sponges. *J. Exp. Mar. Biol. Ecol.* **2008**, *367*, 61−64.
(30) Thiel, V.; Neulinger, S. C.; Staufenberger, T.; Schmaljohann, R.; Imhoff, J. F. Spatial distribution of sponge-associated bacteria in the Mediterranean sponge Tethya aurantium: Sponge-associated bacteria in the sponge Tethya aurantium. *FEMS Microbiol. Ecol.* **2007**, *59*, 47−63.
(31) Goldstein, D. H. *Polarized light*, 3rd ed.; CRC Press: Boca Raton, 2011.
(32) Turtaev, S.; Leite, I. T.; Mitchell, K. J.; Padgett, M. J.; Phillips, D. B.; Čižmár, T. Comparison of nematic liquid-crystal and DMD based spatial light modulation in complex photonics. *Opt. Express* **2017**, *25*, 29874.
(33) Lyu, Z.; Osnabrugge, G.; Pinkse, P. W. H.; Amitonova, L. V. Focus quality in raster-scan imaging via a multimode fiber. *Appl. Opt.* **2022**, *61*, 4363.
(34) Gomes, A. D.; Turtaev, S.; Du, Y.; Čižmár, T. Near perfect focusing through multimode fibres. *Opt. Express* **2022**, *30*, 10645−10663.
(35) Vasquez-Lopez, S. A.; Turcotte, R.; Koren, V.; Plöschner, M.; Padamsey, Z.; Booth, M. J.; Čižmár, T.; Emptage, N. J. Subcellular spatial resolution achieved for deep-brain imaging in vivo using a minimally invasive multimode fiber. *Light:Sci. Appl.* **2018**, *7*, 110.

https://doi.org/10.1021/acsaom.5c00572
ACS Appl. Opt. Mater. 2026, 4, 421−428